Materials & Design 231 (2023) 112042

Contents lists available at ScienceDirect

Materials & Design

journal homepage: www.elsevier.com/locate/matdes

Experimentally validated phase-field model to design the wettability of micro-structured surfaces

Marina Provenzano [a], Francesco Maria Bellussi [a], Matteo Morciano [a], Edoardo Rossi [b], Mario Schleyer [c], Pietro Asinari [a,d], Thomas Straub [c], Marco Sebastiani [b], Matteo Fasano [a,*]

[a] Department of Energy, Politecnico di Torino, Corso Duca degli Abruzzi 24, 10129 Torino, Italy
[b] Universitá degli studi Roma Tre, Department of Engineering, Via della Vasca Navale 79, 00146 Roma, Italy
[c] IWM Fraunhofer, Wöhlerstrasse 11, 79108 Freiburg, Germany
[d] Istituto Nazionale di Ricerca Metrologica, Strada delle Cacce 91, 10135 Torino, Italy

HIGHLIGHTS

- Numerical method to predict the wettability of micro-structured surfaces and assist their design.
- Phase-field model calibration to reproduce the sessile droplet experiment.
- Modelling of several surface morphologies with different intrinsic contact angles.
- Model validation through manufacturing and testing 3D-printed flat and micro-structured samples.

GRAPHICAL ABSTRACT

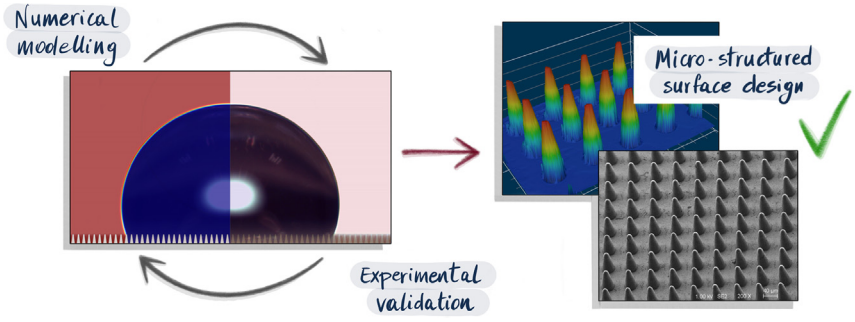

ARTICLE INFO

Article history:
Received 23 December 2022
Revised 15 May 2023
Accepted 25 May 2023
Available online 2 June 2023

Keywords:
Surface engineering
Phase-field model
Wettability
Additive manufacturing
Sessile droplet

ABSTRACT

Surfaces with tailored wettability have attracted considerable attention because of their wide range of potential applications. Wettability can be finely designed by controlling the chemistry and/or morphology of a surface. However, the commonly adopted analytical theories of Wenzel and Cassie-Baxter cannot describe a variety of intermediate and metastable states, being a thorough understanding of the combined chemical and morphological effect on surface wettability still lacking. Hence, the design and optimization of these surfaces is generally expensive and time-consuming. In this work, we propose a numerical method based on the phase-field model to predict the wettability of micro-structured surfaces and assist their design. First, we simulated the sessile droplet experiment on flat surfaces to calibrate model parameters. Second, we modelled several surface morphologies, intrinsic contact angles and droplet impact velocities. Finally, we produced and tested 3D printed flat and micro-structured samples to validate the phase-field model, obtaining a reasonable qualitative and quantitative agreement between numerical and experimental results. The validated model proposed here can help design and prototype surfaces with tailored wettability. Furthermore, integrated with atomistic/mesoscopic simulations, it represents the last step of a predictive multi-scale model, where both chemical and morphological features of surfaces can be designed a priori.

© 2023 The Author(s). Published by Elsevier Ltd. This is an open access article under the CC BY license (http://creativecommons.org/licenses/by/4.0/).

* Corresponding author.
E-mail address: matteo.fasano@polito.it (M. Fasano).

https://doi.org/10.1016/j.matdes.2023.112042
0264-1275/© 2023 The Author(s). Published by Elsevier Ltd.
This is an open access article under the CC BY license (http://creativecommons.org/licenses/by/4.0/).

1. Introduction

Nature offers plenty of examples where fascinating and technologically interesting wettability properties can be observed. Lotus leaves and the wings of some insects (e.g. *Psaltoda claripennis*) exhibit superhydrophobicity and thus unusual self-cleaning properties, which are related to the micro-/nano-scopic surface pattern, together with the low surface energy [1]. Moreover, rose petals, *Terpnosia jinpingensis* wings, and gecko feet exhibit both hydrophobicity and high adhesion [2], causing water droplets to stick to the petal even if it is turned upside down [3]. Such observations have stimulated the design of bioinspired micro- and nano-structured surfaces, resulting from combining different specific chemical compositions and surface morphologies [4,5]. These surfaces can potentially be useful in a wide range of industrial applications [6–8]. Self-cleaning properties can prevent the accumulation of dirt particles on vehicles, walls, shoes or solar cell panels, increasing their efficiency without compromising their optical behavior [9]. Controlling surface properties of materials is also beneficial in water desalination, oil–water separation processes or energy applications [10–13]. Super-hydrophobic coatings can reduce friction resistance, resulting in lower fuel consumption for submarines and boats, thus providing significant environmental benefits [14]. Nanoengineered surfaces can be designed to optimize boiling processes, thus enhancing their heat transfer properties [15]. Last but not least, low free energy surfaces can also be employed in anti-icing systems [16–18].

Micro- and nano-patterned surfaces or superhydrophobic coatings can be manufactured by various techniques, such as nanoimprint lithography, dip-coating, spray-coating, sol–gel process, and chemical vapour deposition [7,19–21]. The fabrication of these surfaces is often expensive and time-consuming, so finding a correlation between the wetting properties of the bulk material and their chemical and geometric features would be extremely useful. The well-known Wenzel and Cassie-Baxter models, which take into account both chemical composition and surface geometry, have often been used as a reference for this purpose [22]. However, several factors involved in defining the equilibrium shape of a droplet on a micro-structured surface are not fully encompassed by these standard models [23–25], thus wettability may be difficult to be assessed a priori.

Various studies have been conducted in the past few years to test the validity of theoretical wettability models and to experimentally verify the possible existence of multiple wetting states for a textured surface (including metastable configurations). On the one side, the experimental results obtained by Shibuichi and co-workers [26,27], Murakami and co-workers [28], and Zhu and co-workers [29] were found to be in qualitative agreement with the Wenzel and Cassie theoretical models. On the other side, experiments conducted by Synytska and co-workers [25] about wetting of textured surfaces were not in accordance with any of the commonly adopted models. Similarly, Mandal and co-workers tested micro/nano hierarchical structured and environment-friendly surfaces [30], which showed hydrophobicity associated with high adhesion, in analogy to the "rose petal effect" [2,3]. In detail, the contact angle – *CA* was increased from $(87 \pm 2)^\circ$ to $(115 \pm 2)^\circ$ after micro-patterning, with roughness factor $r = 3.1 \pm 0.2$ and $\phi_S = 0.43 \pm 0.04$ (being ϕ_S the fraction of the droplet base in contact with the surface), and this behavior could not be explained by Wenzel's theory. Therefore, the debate on the actual reliability of theoretical models of wettability in predicting the full range of possible wetting behaviours is still open [23,24]. Because of the broad variety of the involved phenomena – which complicate theoretical analyses – conducting simulations able to correctly predict the interaction between the droplet and the surface and thus the actual behavior of a properly designed surface has become very attractive. This study aims to support the analysis of wetting behaviors that may fall within or beyond current theoretical descriptions. The Cassie and Wenzel models are used as benchmarks in this work, as they represent a commonly adopted guideline when studying the wettability of non-smooth surfaces.

Contact line motion over a rough or geometrically-structured surface is a complex phenomenon, governed by the presence of moving interfaces and viscous and inertial forces acting at different length scales. When a liquid moves across a solid substrate, the apparent, macroscopically observed *CA* generally differs from the value occurring at equilibrium (static contact angle, *SCA*): the dynamic contact angle (*DCA*) changes during the spreading process, and it is often related to the relative velocity of the three-phase contact line (*TPL*). Different modeling approaches are currently used to study the dynamics of wetting phenomena and to numerically simulate the impact and subsequent propagation of a droplet on an inert surface [31–34]. Considering the classical hydrodynamic model based on Navier–Stokes equations, a non-fixed mesh is generally required to account for the deformation of the droplet shape at the fluid–fluid interface. Moreover, the contact line moves on a solid surface during the spreading process, resulting in energy dissipation. The boundary condition (*BC*) commonly used in this model at the solid–fluid interface is the no-slip one, which, however, may lead to a stress singularity at the moving *TPL* when hydrodynamic conditions are simulated. Many strategies can be followed to avoid this singularity and thus enable the use of a sharp-interface hydrodynamic model [35], such as employing a slip condition at the wall. When geometrically structured surfaces are present, however, the contact line is subject to multiple reconfigurations, and complex resolution algorithms are required [36,37]. An alternative way to study multiphase flows and interface problems without requiring moving meshes is to use diffuse-interface models (*DIM*), such as the phase-field model (*PF*) [38–40]. These methods can predict the *TPL* movement on solid substrates without causing stress singularities, being therefore suitable for simulating wetting phenomena of structured solid surfaces. Diffuse-interface methods replace the sharp interface (separating two different phases in the hydrodynamic approach) with a transition region of finite thickness, through which physical properties undergo a rapid but smooth and continuous change. This expedient simplifies the numerical handling of changes in complex interface topology: the fluid separation surface is no longer a domain boundary, so its position does not have to be explicitly defined at each simulation time step, because the equations are solved over the entire domain. However, since these models involve fourth-order differential equations, the computational costs required for their implementation are higher than those of traditional methods. Furthermore, the use of these models entails limitations due to the non-zero thickness of the interface and the mass losses that may occur [36,37,41]. *DIM*s can either use an interface thickness justified by purely numerical grounds, as in the level-set (*LS*) [42] or volume of fluid (*VOF*) methods [43,22], or they can physically correlate the interface thickness with the chemical potential of fluids and their free energy, as in the Cahn–Hilliard phase-field model. Nevertheless, to the best of the Authors' knowledge, Cahn–Hilliard phase-field model has never been adopted to predict the wettability of micro-structured surfaces, at least when moving droplets are concerned.

Here, the wettability of micro-structured surfaces was investigated by means of numerical simulations validated by experimental measurements. A diffuse interface phase-field model based on the Cahn–Hilliard equation was chosen, allowing a moving, deformable surface to coexist with a fixed mesh. Such model was found to be stable, as it removes the singularity at the contact line, and less sensitive to numerical parameters than the level-set

method [44], since the finite thickness of the interface is not merely justified by numerical considerations but relies on physics.

2. Materials and methods

2.1. Governing equations

According to the Cahn–Hilliard equation [38], which relies on the Van der Waals free energy density formulation for isothermal fluids [45], the free fluid–fluid mixing energy density [39] can be expressed as:

$$f_m(\phi,\nabla\phi)=\frac{\lambda}{2}|\nabla\phi|^2+\frac{\lambda}{4\epsilon^2}(\phi^2-1)^2, \tag{1}$$

where ϕ is the phase-field variable, λ is the mixing energy density, and ϵ is the capillary width, which scales with the thickness of the interface [39]. The first term on the right-hand side of Eq. 1 represents a "philic" effect, which is due to the interactions between the components that tend to create a complete mixing. The second term on the right-hand side, instead, identifies a "phobic" effect, which is associated with a total separation of phases into pure components ($\phi=\pm1$) and results in the classical sharp interface. Then, $\frac{(\phi^2-1)^2}{4}$ represents the Ginzburg–Landau double well potential for the phobic free energy and accounts for the immiscibility of fluid components. At equilibrium, the fluid–fluid interfacial tension σ is given by [38,39]:

$$\sigma=\frac{2\sqrt{2}}{3}\frac{\lambda}{\epsilon}. \tag{2}$$

The free energy for a given domain Ω can be then written as $F=\int_\Omega f_m(\phi,\nabla\phi)d\Omega$, whereas the chemical potential is the rate of change of F with respect to ϕ (functional derivative), namely:

$$G=\frac{\delta F}{\delta\phi}=\frac{\lambda}{\epsilon^2}(\phi^2-1)\phi-\lambda\nabla^2\phi. \tag{3}$$

According to Fick's law, the flux density of the diffusing species is proportional to the concentration gradient by an appropriate coefficient, and its movement is gradient-adverse. Generalizing this law, it is possible to relate the flux to the chemical potential gradient, resulting in an advection–diffusion equation [38,46]:

$$\frac{\partial\phi}{\partial t}+\boldsymbol{u}\cdot\nabla\phi=\nabla\cdot(M\nabla G), \tag{4}$$

where $M=\chi\epsilon^2$ is a phenomenological mobility parameter and χ is the mobility tuning parameter, which determines the time scale of diffusion (i.e., the relaxation time of the interface), and $\boldsymbol{u}$ the velocity field. If M is excessively large, the convective term is overdamped; at the same time, it needs to be sufficiently high to counteract straining flows that would otherwise cause changes in the interface thickness. To simplify the numerical resolution, Eq. 4 was split into two second-order *PDE*s by the use of an auxiliary variable ξ:

$$\frac{\partial\phi}{\partial t}+\boldsymbol{u}\cdot\nabla\phi=\frac{\lambda M}{\epsilon^2}\nabla^2\xi \tag{5}$$

$$\xi=(\phi^2-1)\phi-\epsilon^2\nabla^2\phi. \tag{6}$$

The Navier–Stokes equations are then modified to account for the presence of an interface, including a body force ($G\nabla\phi$) transformed via the divergence theorem to represent the surface tension:

$$\rho\left(\frac{\partial\boldsymbol{u}}{\partial t}+\boldsymbol{u}\cdot\nabla\boldsymbol{u}\right)=-\nabla p+\nabla\cdot\mu[\nabla\boldsymbol{u}+(\nabla\boldsymbol{u})^T]+G\nabla\phi+\boldsymbol{F}. \tag{7}$$

In Eq. 7, $G\nabla\phi$ is non-zero only within the interface region, where the gradient has a finite value. Moreover $\boldsymbol{F}$ accounts for gravity or buoyancy. Density ρ and viscosity μ used for calculations can be expressed as [46]: $\rho=\frac{1}{2}[(1-\phi)\rho_1+(1+\phi)\rho_2];\ \mu=\frac{1}{2}[(1-\phi)\mu_1+(1+\phi)\mu_2]$. Similarly, referring to volume fractions $V_{f1}=\frac{1-\phi}{2}$ and $V_{f2}=\frac{1+\phi}{2}$ [41]:

$$\rho=\rho_1V_{f1}+\rho_2V_{f2};\ \mu=\mu_1V_{f1}+\mu_2V_{f2}, \tag{8}$$

where subscripts 1 and 2 identify the two phases, respectively. Here, the finite element analysis software COMSOL Multiphysics® was chosen for the resolution of these *PDE*s [22,47].

2.2. Boundary conditions

First, a null perpendicular velocity component of the fluid occurs at a non-permeable solid wall, i.e.:

$$(\boldsymbol{u}-\boldsymbol{u}_w)\cdot\boldsymbol{n}=0, \tag{9}$$

where $\boldsymbol{u}_w$ is the boundary velocity ($\boldsymbol{u}_w=\boldsymbol{0}$ for a fixed wall) and $\boldsymbol{n}$ is the outward-pointing normal unit vector. Moreover, when a viscous fluid is in proximity to a surface, the fluid is generally assumed to adhere to the wall and thus have the same velocity as the domain boundary. This assumption results in the following expression:

$$(\boldsymbol{u}-\boldsymbol{u}_w)\cdot\boldsymbol{t}=0, \tag{10}$$

where $\boldsymbol{t}$ is a general unit vector tangential to the wall. However, such no-slip condition represents a problem if a moving interface is in contact with a solid surface, as in wetting phenomena: in such circumstances, the adoption of a hydrodynamic model combined with this condition may lead to a stress singularity at the *TPL*, which could be overcome by discrete models [48]. This problem can be bypassed also at the continuum scale via a phase-field model, since the diffusion introduced by the Cahn–Hilliard equations allows for contact line motion, even when a zero velocity field occurs. The coexistence of a moving contact line and a condition of adherence to the wall might seem a paradox – partially explained by the fact that the diffusive flow is not actually a macroscopic flow – but it is rather due to molecular displacements that occur on a microscopic scale [49]. Although other boundary conditions (such as Navier *BC – NBC* or Generalized Navier *BC – GNBC* [22]) sometimes provide a more accurate description of the physics actually involved in liquid–solid interaction, the no-slip condition is a good option when diffuse-interface methods are used and computational time has to be reduced [41].

A phase-field model includes the variable ϕ, which therefore requires appropriate boundary conditions. When a fluid is in contact with an impermeable wall, no diffusive flux across the surface is observed, that is:

$$\boldsymbol{n}\cdot\nabla G=0. \tag{11}$$

Moreover, an instantaneous equilibrium between fluid and solid wall is typically supposed, imposing a dynamic microscopic contact angle equal to the static equilibrium value [41,49]:

$$\cos\theta_S=\frac{\boldsymbol{n}\cdot\nabla\phi}{|\nabla\phi|}. \tag{12}$$

This approach is a specific case of a more general boundary condition, which takes non-equilibrium states into account and allows for the emergence of a dynamic microscopic contact angle θ_D, different from the static contact angle θ_S during flow [50]:

$$\frac{\partial\phi}{\partial t}+\boldsymbol{u}\cdot\nabla\phi=-\Gamma L(\phi), \tag{13}$$

where L is the surface chemical potential, while Γ is a rate constant depending on material properties; however, the values of these parameters are often not known, so they are mostly treated as phenomenological parameters.

In this work, a no-slip non-penetration condition was imposed at the solid wall, resulting in zero fluid velocity next to the solid substrate (Fig. 1a). *NBC* and *GNBC* were not chosen for several reasons, including the desire to fully exploit the advantages introduced by the phase-field model, as well as to reduce computational time, which would have inevitably increased by adopting more complex formulations. Moreover, slip models of *NBC* and *GNBC* use a characteristic length, l_s, which would have added a further degree of freedom to the system. It is also worth mentioning that these models involve very small length scales and fail in the vicinity of the contact line. Furthermore, the main interest here was not about the process dynamics, but rather about the stationary condition achieved at the end of the transient simulation, similarly to previous works [41,50].

Analogous reasoning led to the choice of boundary conditions for the phase-field variable ϕ: a rigorous approach would have required the use of Eq. 13 and so the introduction of Γ parameter, which is generally unknown. As also explained in [22], it is possible to recover the correct macroscopic solution by properly using mutual compensation between the effects related to M and Γ. In order to obtain this result, however, it would be necessary to know the true values of these two parameters, or to perform a fitting on experimental data, which are not usually available [50]. For these reasons, a microscopic contact angle equal to the static value was imposed, using Eq. 12 in conjunction with 11 (no flux through the wall). It is worth specifying that the application of Eq. 12 in numerical simulations actually corresponds to imposing a macroscopic contact angle, since the grid size is much greater than the typical length scales of the region immediately adjacent to the contact line. For this reason, some authors neglect the inner region next to the *TPL* and apply a dynamic model to the contact angle through Eq. 12, therefore imposing that the apparent contact angle, defined as $\cos\theta_a = \frac{\boldsymbol{n}\cdot\nabla\phi}{|\nabla\phi|}$, follows equations such as Cox's or molecular kinetic theory [22,41]. Such an approach, however, besides increasing the system degrees of freedom and the computational time, introduces an explicit link between angle and contact line velocity, which cannot be assessed with respect to the fluid velocity, having imposed a no-slip condition at the wall. Again, being mostly interested in the steady state achieved, we preferred to impose a constant contact angle equal to the static value. Some previous results indeed highlighted that this boundary condition fails to properly model the dynamics of the spreading process, but it can satisfactorily predict the equilibrium droplet shape [41]. For the sake of clarity, it should be specified that the macroscopic contact angle discussed in this paragraph refers to length scales comparable to the mesh size; henceforth, by apparent contact angle we will refer to that macroscopically observed, assessed at some distance from the wall, such that it is not affected by edge effects due to the imposed boundary conditions. For more details about the chosen boundary conditions, see [22].

2.3. Simulation protocol

We initially simulated the equilibrium contact angle of a droplet on a perfectly smooth surface to assess the physical consistency of the model in a simple case. We adopted a half two-dimensional symmetrical domain, due to the high computational costs that would be required by a full three-dimensional domain (see [22] for further details). The droplet was placed a few tenths of a millimeter (depending on the mesh size and interface thickness used) from the surface at time zero, so as to minimize the duration of the transient phase. This choice also reduced the computational time and prevented from being influenced by impact velocity. We used a water droplet with a radius R = 1 mm, so that the characteristic length of the system would be smaller than the capillary length l_c (in the case of water at 20°C, l_c = 2.71 mm), to avoid possible effect of gravity and guarantee the spherical shape of the droplet. The droplet was placed at a distance of at least 2 mm from the upper and right boundaries to ensure that the open boundary conditions imposed did not affect the deformation of the interface.

The choice of a diffuse-interface model avoided the use of a moving computational grid, so a fixed triangular non-uniform mesh was adopted. Mesh properties can be defined by several parameters, such as the mesh element size h, i.e., the length of the longest edge of the element. The mesh is overall characterized by a maximum element size h_{max}. The area crossed by the interface motion was subdivided into finer elements than the remaining part of the domain (see Fig. 1b), since in phase-field methods the mesh size is closely related to the interface thickness, but at the same time the reduction of the mesh size increases the computation time [44,51]. We assumed the absence of relevant turbulent dissipation and chose a laminar flow model. Indeed, the starting condition considered for the simulations is close to equilibrium and the fluid motion is characterized by low velocities. Thus, we implemented the continuity equation ($\nabla \cdot \boldsymbol{u} = 0$) and the Eq. 7, coupled to Eqs. 5 and 6 through Eqs. 3 and 8. All phenomena related to flow compressibility, thermal effects and surface tension gradients were neglected; the gravitational term in the Navier–Stokes equations was included to model droplet deposition. Reference pressure and temperature were set to p_{ref} = 1 atm and T_{ref} = 293.15 K,

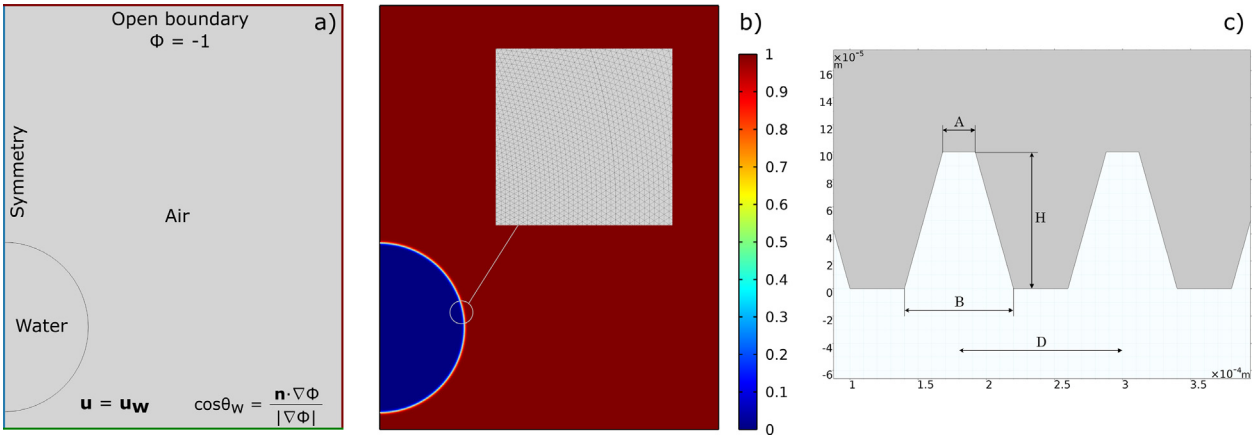

Fig. 1. (a) Computational domain and boundary conditions used. (b) Simulation domain at the initial condition. The color bar indicates the air volume fraction (see Eq. 8). (c) Geometry of the micro-structured surface with details of the characteristic dimensions.

respectively. We referred to the air and water phases in Eq. 8 as "Fluid 1" and "Fluid 2", respectively.

To evaluate the resulting apparent contact angles, we approximated the air–water interface near the *TPL* in the 2D-domain with a straight line passing through two sufficiently close points [22], exploiting the definition of tangent to a curve. The contact angle was measured slightly offset from the solid wall to avoid any local effects due to the mesh or domain boundary. The results of this procedure were substantially in agreement with the imposed boundary conditions on the wetted wall, confirming the reliability of the simulations performed. We then repeated the procedure while reducing the mesh size and checked that the results were not significantly affected by changes in interface thickness. Indeed, the interface width of real systems is much smaller than that used in numerical approximations. During the simulation we extracted the profile of V_{f2} along an horizontal line at each time-step, to identify the evolution of the *x*-coordinate of the interface; the same procedure was applied along the *y*-axis. The positions thus identified exhibited oscillatory trends along the simulation until equilibrium, when the *CA* was evaluated [22]. For each simulation, we also checked the conservation of mass to ensure the quality of the numerical results. The water mass per unit volume can be defined as: $\rho_{\text{water}} = \rho_2 \cdot V_{f2}$.

We then added trapezoidal micro-structures on the solid surface, to analyze the effect of morphological features on surface wettability [52,53]. The micro-structure can be described through geometric parameters such as the size of the upper base *A*, the lower base *B*, the height *H* and the distance between two trapezoids *D* (see Fig. 1c), as well as the surface roughness factors *r* and ϕ_S (parameters of the theoretical wettability models). To explore the effect of chemical and morphological surface features on their wettability response, different *CA*s and micro-structured topologies were simulated.

2.4. Model calibration

The two parameters of the interface model are the interface thickness ϵ and the mobility parameter *M*. ϵ must be large enough to ensure a smooth ϕ profile to adequately reflect the diffusive nature of the model [46]. Too high values, on the other hand, could compromise the reliability of simulations, especially if the interface interacts with geometric structures of comparable size to its own thickness: in that case, the result would depend on the value of ϵ and thus the solution would have no physical relevance, even if numerically acceptable. At the same time, it is worth recalling that the width of interfaces typically considered in simulations is much larger than those of real physical systems, since realistic thicknesses could not be handled with current computational resources [41]. In fact, this thickness is closely related to the mesh size: to properly capture the surface profile, the grid must have dimensions at least comparable to ϵ [50]. Previous works [46] suggest using an interface thickness equal to or larger than half the mesh size; therefore, we chose to compare the results obtained with different ϵ values in order to select the most appropriate thickness [22]. *M*, instead, governs the time scale of diffusion in the Cahn–Hilliard equations, and it is related to ϵ by the mobility tuning parameter χ. *M* must be large enough to keep the width of the interface constant, but if too large it may overly dampen convective motion [46]. Hence, the choice of these parameters significantly influences simulations, as well as whether or not the result is independent of the interface thickness (i.e., whether the sharp-interface limit is reached).

We decided to treat mobility, in particular χ and ϵ, as phenomenological parameters. We performed several simulations with a smooth surface, imposing a wall contact angle of *CA* = 120° and systematically changing the mesh size h_{max} (hence the interface thickness ϵ) and the parameter χ. For each simulation, we analyzed the final contact angle obtained, and checked the conservation of mass and the achievement of a sufficiently stable state (variations of the interface positions with respect to the *x* and *y* axes less than 2%). All the simulations carried out resulted in a final *CA* consistent with the imposed boundary conditions (discrepancy between imposed and obtained contact angle almost constant and less than 5%), so it could not be used alone as a benchmark to assess the quality of results. We therefore analyzed also the error related to the conservation of water mass, the computational costs and the stability of simulations, and chose the value of χ optimizing these figures of merit ($\chi = 100$ m s/kg in this work) [22].

Instead, achieving a ϵ-independent solution (i.e., convergence to the sharp-interface limit) in domains characterized by micro-structured surfaces is not trivial: interactions between geometric entities with length scales comparable to the interface thickness and the interface itself lead to an upper limit for the ϵ values (i.e., mesh sizes) that can be used, thus tightening the convergence criterion. In contrast to what was observed with smooth surfaces, not all meshes used for these simulations led to results independent of the interface width. For each geometrical configuration analyzed, we then progressively decreased the maximum size of the mesh elements (as well as ϵ) while keeping the other model parameters unchanged, and then evaluated the obtained apparent contact angle, thus verifying the independence of results from the considered ϵ (Supplementary Fig. S1). Again, water mass conservation and stability of the achieved state were verified (Supplementary Figs. S2 and S3). More information about this calibration procedure can be found in [22].

2.5. Sample preparation

Samples consisting of either arrays of truncated cones or a flat pad were printed via 3D laser lithography systems, using two-photon-polymerization (see Fig. 2a). Sample configurations were designed using a commercial CAD software (Autodesk® Inventor®) and were exported as stereolithography files. The characteristic geometrical parameters of the samples are shown in Table 1.

The NanoOne printer and the UpPhoto resin (UpNano©) were used to produce samples. The photoresist was placed in a vat with a precision glass window at the bottom. The vat was mounted rigidly above the lens. Its glass window helps to preserve the focusing power of the lens. During printing, the lens and vat move further down from the substrate after each layer. Thus, the structure is pulled out of the photoresist in the vat. The selected setting parameters are shown in Table 2. All samples were printed on conventional laboratory glass, as substrate. The geometry of the cone-shaped printed samples was analyzed by 3D laser scanning. In detail, a Keyence VK9700K 3D laser scanning microscope was used, with setting parameters shown in Table 3. The actual geometry was measured by generating line profiles along the *x* and *y* axes, crossing the maxima or the top of each cone (see Table 3 and Fig. 2b). For each sample, a subsection of 4×3 cones was scanned from the considered array.

2.6. Experimental characterization

Both the micro-patterned and the reference flat 3D printed surfaces were tested to assess their properties and the wetting state achieved. A normative-compliant equipment (UNI EN 828, UNI 9752, ASTM D-5725–99) was employed to perform sessile drop tests over the samples, and thus measure the apparent static (θ_S), advancing (θ_A) and receding (θ_R) contact angles [22]. For each of the cases examined, at least five droplets of deionized water were

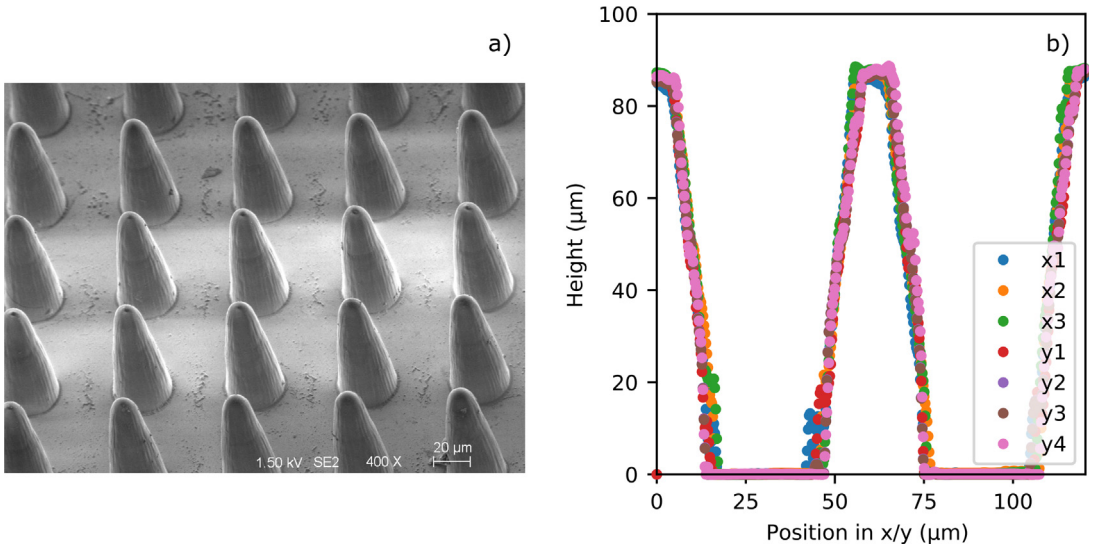

Fig. 2. (a) Scanning Electron Microscope overview of the micro-structured sample. (b) 3D laser scanning analysis of the micro-structured sample (see Table 3 for details on used parameters). Different colours refer to the scanning axes used. The latter were chosen according to the positioning of the truncated cones (i.e., 3 distributed along the x-axis and 4 along the y-axis). Note that the top of the cone is actually curved, but laser profilometry shows an almost trapezoidal shape due to light scattering phenomena at the cone tip.

Table 1
Overview of geometrical parameters of the manufactured samples. *a* and *h* are the side dimension and thickness of the flat sample, respectively.

	Parameters (µm)						
	A	B	D	H	a	h	Array
Cone	12	40	60	100	–	–	84×84
Flat pad	–	–	–	–	5000	200	–

Table 2
Setting parameters for printing the samples by NanoOne.

Parameter	Value
Lens magnification/NA	10×/0.4
Laser power	50 mW
Speed	600 mm s^{-1}
Hatching (x-y-plane)	0.5 µm
Slicing (z direction)	5 µm

Table 3
Setting parameters adopted for profilometry.

Parameter	Value
Lens magnification/NA	50×/0.95
z-increment	0.5 µm
xy-calibration	276 nm/pixel
z-calibration	1 nm/digit

deposited at 20°C temperature and relative humidity between 40% and 50%. A droplet volume of 4.1 µL was selected so that volume forces (i.e., gravitational effect) would not significantly affect wettability while still allowing the drop to interact with a relevant set of micro-cones, as well as to ensure radius values comparable to those used for simulations.

To assess the static contact angles associated with flat and micro-structured surfaces, drops of water were deposited on each sample [54]. After 60 s of stabilization, images of the liquid drops were captured (LAS-EZ software, Leica Camera AG) and subsequently processed (ImageJ software) using a spherical approximation of the droplet shape. For the micro-structured sample, the surface formed by joining the upper portions of the cones was considered as the liquid–solid interface, thus allowing the evaluation of the apparent contact angle. Measurements of θ_A and θ_R contact angles were made according to the same testing conditions as those employed for static angles. Experiments were performed using a goniometer stage (Thorlabs GN2/M) with pure rotational motion (backlash-Free Spring-Loaded design) over two axes, so that both flat and micro-structured samples were positioned at a tilt angle of 15 degrees. In the case of the micro-structured surface, an additional 90-degree tilting condition was also investigated using a vertical sample holder. The procedure involved depositing a droplet on the sample surface and then tilting the goniometer stage/sample holder to achieve the desired tilting angle, while minimizing contact line changes produced by vibrations as much as possible.

The acquired images were then post-processed with ImageJ, and the contact line projection and liquid–solid interface were manually interpolated so that contact angles could be calculated. Since this method exploits gravity, the volume of the droplets becomes a meaningful parameter, so the analysis was repeated using 10 µL drops (higher volumes could not be used because of the finite surface area available for measurements). The CA values obtained with the two different volumes were found to be comparable, so only the results for 4.1 µL drops are reported and further discussed below.

3. Results and discussion

Some representative simulation results showing different wetting states on the micro-structured solid surfaces are displayed in Fig. 3. Wenzel (Fig. 3a and b) or Cassie-Baxter (Fig. 3c) states were observed depending on the simulated geometry of the

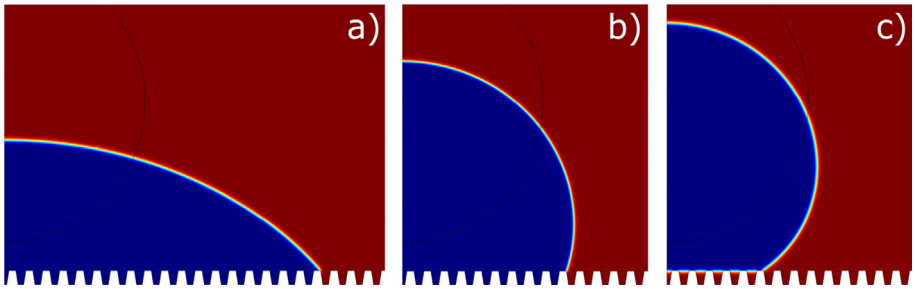

Fig. 3. Numerical wetting states on a micro-structured solid surface, which is characterized by A = 48 μm, B = 80 μm, D = 120 μm, and H = 100 μm. A Wenzel state is obtained with intrinsic contact angle CA_w equal to (a) 30° and (b) 70°; (c) a Cassie-Baxter state with CA_w equal to 120°. Different colors identify the fraction of air in the domain: blue corresponds to $V_{f1} = 0$ ($\phi = 1$), red to $V_{f1} = 1$ ($\phi = -1$, see Fig. 1). The black circle identifies the water droplet position at time zero.

micro-structure, as well as the intrinsic contact angle CA_w imposed at the solid wall (i.e., θ_Y in Figs. 4 and 5). Without loosing generality, these wetting states were obtained considering a micro-structured surface characterized by A = 48 μm, B = 80 μm, D = 120 μm, H = 100 μm and contact angle equal to 30°, 70° and 120°, respectively.

Several simulations were carried out, varying the intrinsic contact angle and the geometry of the micro-structure (further images are provided in Supplementary Figs. S4 and S5). In detail, as reported in Fig. 4, four different micro-structures were considered, namely (a) A = 24 μm, B = 80 μm, D = 120 μm, and H = 200 μm (Fig. 4a and Supplementary Table S1); (b) A = 24 μm, B = 80 μm, D = 120 μm, and H = 100 μm (Fig. 4b and Supplementary

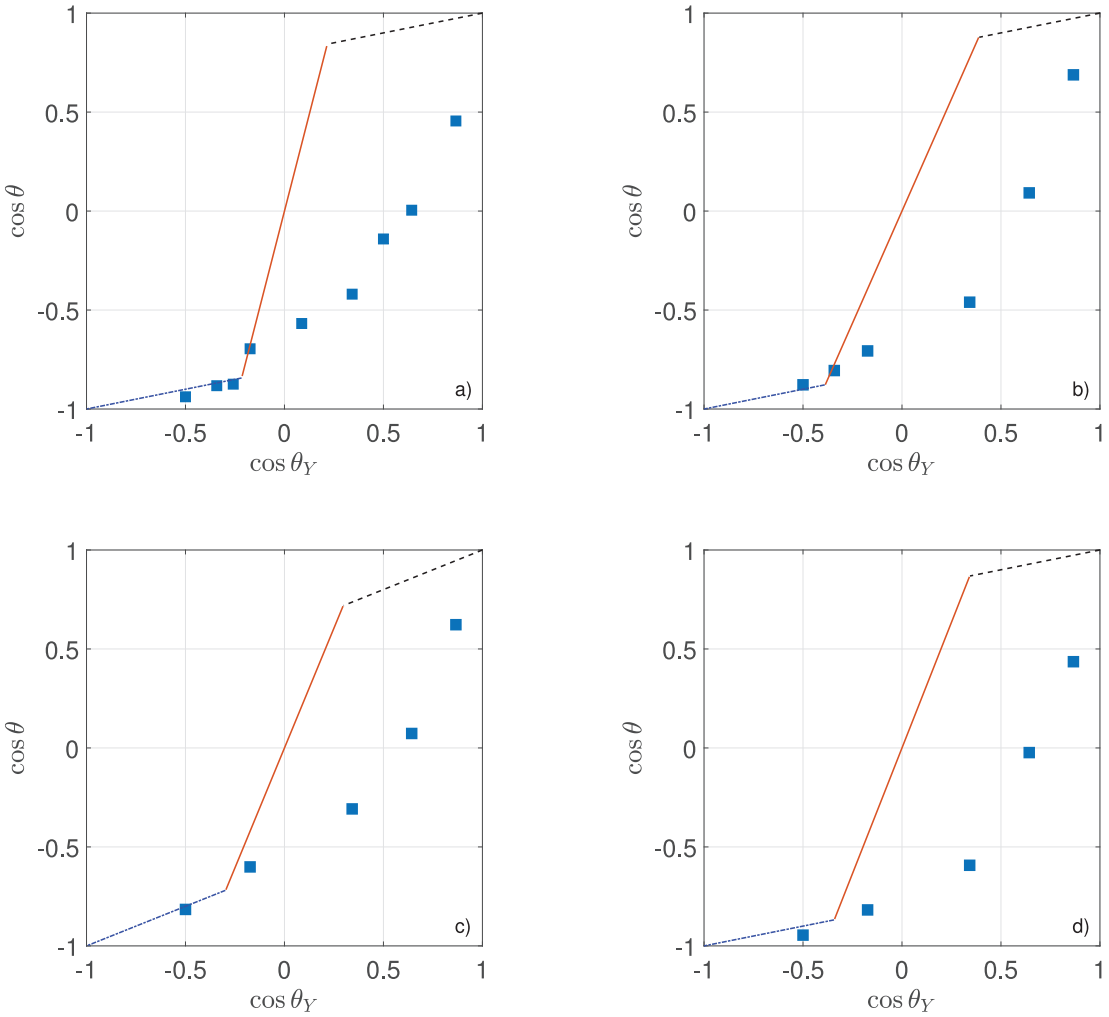

Fig. 4. Comparison between simulations and theoretical equations. Blue squares represent numerical data, the dashed blue line describes the Cassie-Baxter model, the orange line represents the Wenzel equation, and the dashed black line stands for the Wet Cassie state. The x-axis shows the cosine of the intrinsic contact angle (θ_Y), while the y-axis displays the cosine of the apparent contact angle (θ). (a) A = 24 μm, B = 80 μm, D = 120 μm, H = 200 μm (Supplementary Table S1); (b) A = 24 μm, B = 80 μm, D = 120 μm, H = 100 μm (Supplementary Table S2); (c) A = 48 μm, B = 80 μm, D = 120 μm, H = 100 μm (Supplementary Table S3); (d) A = 48 μm, B = 80 μm, D = 240 μm, H = 200 μm (Supplementary Table S4).

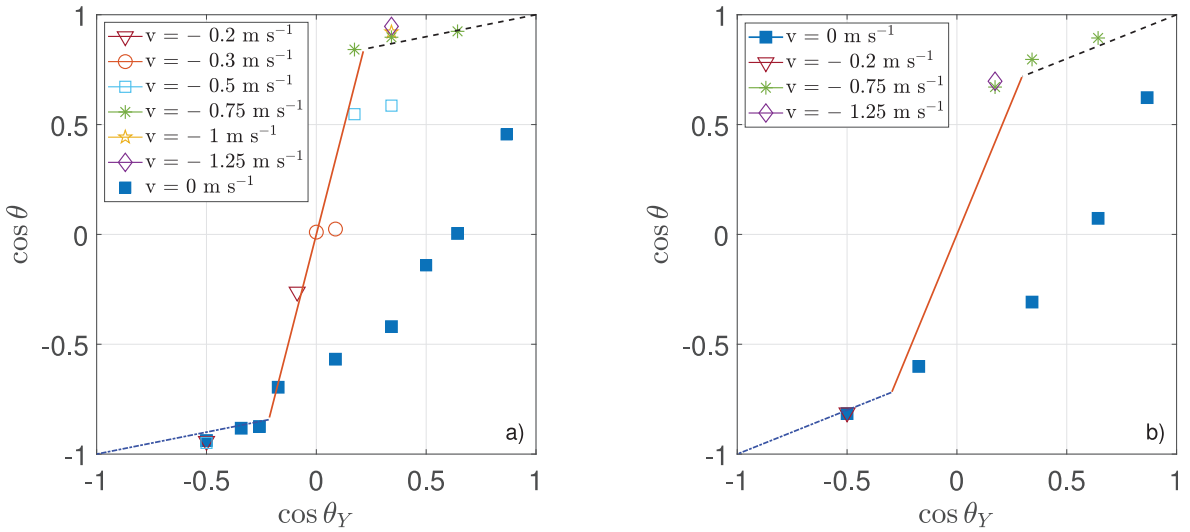

Fig. 5. Comparison between simulations and theoretical equations, at different droplet initial velocities. The dashed blue line describes the Cassie-Baxter model, the orange line represents the Wenzel equation, and the dashed black line stands for the Wet Cassie state. The x-axis shows the cosine of the intrinsic contact angle (θ_Y), while the y-axis displays the cosine of the apparent contact angle (θ). (a) A = 24 μm, B = 80 μm, D = 120 μm, H = 200 μm (see Supplementary Table S5, for further details); (b) A = 48 μm, B = 80 μm, D = 120 μm, H = 100 μm (see Supplementary Table S6, for further details).

Table S2); (c) A = 48 μm, B = 80 μm, D = 120 μm, and H = 100 μm (Fig. 4c and Supplementary Table S3) and (d) A = 48 μm, B = 80 μm, D = 240 μm, and H = 200 μm (Fig. 4d and Supplementary Table S4).

By comparing the numerical results (see blue squares in Fig. 4) with the theoretical predictions by Wenzel and Cassie equations (see lines in Fig. 4), it can be appreciated how simulations faithfully reflect the theoretical predictions only at high intrinsic contact angles, which characterize the Cassie-Baxter state and the Cassie-Wenzel transition. In these cases, micro-structures increase the surface hydrophobicity, resulting in an apparent contact angle higher than what would be obtained with a smooth surface. This behavior is due to the presence of air pockets trapped in the micro-structure grooves, which suspend the droplet over the bottom surface. Decreasing θ_Y results in a transition to the Wenzel state, with water completely filling the micro-cavities. This transition is reproduced with reasonable accuracy by simulations, as shown more prominently in Fig. 4a. By further reducing the wall intrinsic contact angle, however, the numerical values deviate significantly from Wenzel's theory, since it does not predict that an intrinsically hydrophilic surface may become hydrophobic due to the presence of micro-structures, as observed in simulations instead. The maximum discrepancy is achieved with intrinsic contact angles of around 70°, and the mismatch concerns the value of the apparent contact angle: in the simulations, water penetrates the cavities of the micro-structure, as predicted by Wenzel's theory. Moreover, increasing the height of the cones reduces the matching between numerical and theoretical results. It is worth noting, though, how the overall qualitative behavior of the system remains nearly invariant for the different micro-structures simulated. The size of the micro-structures, on the other hand, affects the value of the apparent contact angle (θ) that is obtained with a specific intrinsic contact angle (θ_Y), as well as the mesh size below which the result is no longer ϵ-dependent (see Supplementary Tables S1-S4).

One of the reasons behind the observed discrepancies between numerical and theoretical results may lie in the non-exhaustiveness of Wenzel and Cassie's theories, already pointed out several times over the years [25,30]. In fact, these theories represent a commonly accepted guideline for wetting phenomena involving non-smooth surfaces, but they are unable to catch many aspects of them since, e.g., they do not take into account the actual geometry of the surface but only certain roughness factors, which may be not sufficient to analyze the multitude of possible behaviors. As a matter of fact, according to the theoretical model, an inherently hydrophilic surface with increasing roughness may only improve its natural wetting properties; similarly, a suspended state may only be achieved with intrinsically hydrophobic materials. However, this description is not exhaustive, as shown by experimental data [25,30,55] and simulation results reported by other authors [36], since other possible wetting states exist, including metastable ones. Synytska et al. [25], in particular, observed that their experiments did not follow any of the models studied, and the deviation from the Wenzel and Cassie equations increased as the intrinsic contact angle decreased. This behavior can be justified by assuming the existence of a multitude of metastable configurations for a droplet on a rough surface, each separated from the adjacent one by an energy barrier.

In light of this, additional tests were performed imposing a non-zero kinetic energy on the drop at the initial instant of simulation. Micro-structured surfaces characterized by (a) A = 24 μm, B = 80 μm, D = 120 μm, H = 200 μm or (b) A = 48 μm, B = 80 μm, D = 120 μm, H = 100 μm were considered, and initial droplet velocities between 0.2 m s^{-1} and 1.25 m s^{-1} were selected, with results reported in Fig. 5. For high intrinsic contact angles, corresponding to numerical results already in agreement with the Cassie-Baxter theory, considering a non-zero initial velocity does not significantly alter the final configuration: these outcomes suggest that the condition achieved is a stable state. At lower intrinsic contact angles, on the other hand, the presence of an impact velocity allows the attainment of a final state different from the one previously obtained and more in agreement with the theoretical predictions (see Supplementary Figs. S6 and S7 and Supplementary Tables S5 and S6 for further details). The energy required to achieve this result increases as the wall contact angle θ_Y decreases; moreover, the change in the resulting apparent contact angle appears to be increasingly less pronounced as kinetic energy increases. Without any claim to universality, these outcomes would seem to confirm the hypothesis of metastable states, since by introducing a perturbation into the system the condition reached is altered. The results obtained with both geometries were consistent with each other, demonstrating comparable behaviors

and thus generality of the resulting remarks (cf. Figs. 5a and b), at least for the considered configurations.

A flat and a micro-structured experimental sample (made of the same polymeric material) were produced and tested to validate the observed simulation results. The actual geometric dimensions of the micro-structure were assessed by analyzing the profiles obtained from the 3D laser scanning (see Section 2.5 for further details), and they are slightly different from those intended (Table 4). Table 5 displays the results of contact angle tests performed on the different samples. Static contact angle values relative to the flat surface reveal the hydrophilic behavior of the specimen material (θ_S = 70.4° ± 1.8°). On the other hand, the introduction of the surface micro-structure results in the sample being hydrophobic, as shown by the apparent contact angle obtained with the patterned surface (θ_S = 107.4° ± 4.5°, Fig. 6a). A more detailed analysis of the experimental images in Fig. 6b also reveals that water penetrates the gaps between the micro-structures below the droplet, although it is not possible to assess whether it fills this space completely or rather creates fluid-gas interfaces between the cones. The absence of air pockets interposed between the fluid and the surface would also seem to be confirmed by the experiments concerning advancing and receding contact angles. Even when tilting the micro-structured sample at a 15 or 90 degree tilt angle, the drop remains attached to the sample and does not slide over the surface (in contrast to what would happen with a Cassie-Baxter state); the same behavior can be observed when turning the specimen upside down. Comparing the values of the static, advancing and receding angles of the micro-structured sample also shows that both θ_A and θ_R are smaller than θ_S, while generally $\theta_R < \theta_S < \theta_A$. This result can be interpreted by assuming that, due to gravity, the contact line highly deforms and the drop interacts with the surrounding pillars, but without slipping or detaching itself from the surface. To summarize, the experiments show that the flat surface is hydrophilic, while the micro-structured sample (made of the same material) is hydrophobic; moreover, the behavior of the patterned surface is not consistent with a Cassie-Baxter suspended state, but rather with fluid penetration throughout the micro-structures (limited to the area below the drop).

Some simulations were then run considering micro-structure dimensions comparable to those of the test specimens and without initial velocity (see Fig. 6c and Supplementary Table S7), for a fair numerical-experimental comparison. The numerical results obtained from this analysis are consistent with the behavior shown by previously simulated micro-structures (blue squares in Figs. 4 and 5). In agreement with experimental data, simulations reveal a hydrophobic behavior for the micro-structured surface, even when an intrinsic hydrophilic contact angle is imposed at the wall. As reported in Fig. 6c, the numerical and experimental values of the contact angle differ by about 12%. This discrepancy may be ascribed to both experimental measurement uncertainties (e.g., the sample geometry is not exactly a truncated cone, the surfaces are not perfectly smooth, the drop is unavoidably perturbed during tests) and simulation approximations (e.g., not having used a dynamic condition for the contact angle in the phase-field model and having adopted a 2D model). Furthermore, a qualitative analysis of the numerical equilibrium condition appears to confirm consistency with the experiments: simulations show that water penetrates the space between the micro-structures in the area below the droplet, without the formation of air pockets (Wenzel-like state). Finally, theoretical models indicate that the tested sample should be in a Wenzel state, with an apparent static contact angle of θ = 38° (see Fig. 6c). This consideration, however, is not consistent with the experimental (and numerical) data, since a hydrophobic apparent contact angle of 107.4° ± 4.5° is observed.

The simulations chosen for this work do not claim to be representative or predictive of all observable behaviors in nature, especially since two-dimensional domains are used. The employment of 2D simulations does indeed overcome the high computational costs related to 3D models, although leading to some inaccuracies in the description of phenomena. However, it could be a valuable aid in the design of micro-structured surfaces and could help compensating for the non-exhaustiveness of current theories.

Table 4
Characteristic dimensions of the micro-structured surface produced, as from profilometry data (see Fig. 1c for the definition of geometrical parameters).

Parameter	Target value (μm)	Real value (μm)
A	12	8.3 ± 0.9
B	40	30.4 ± 1.9
D	60	60.1 ± 0.1
H	100	87.1 ± 1.3

Table 5
Experimental values of contact angles obtained for the flat and micro-structured samples (θ_S: static *CA*; ,$\theta_{A/R,15°}$: advancing and receding *CA*s obtained at a 15 degree tilt; $\theta_{A/R,90°}$: advancing and receding *CA*s obtained at a 90 degree tilt).

	Flat	Micro-structured
θ_S (°)	70.4 ± 1.8	107.4 ± 4.5
$\theta_{A,15°}$ (°)	73.6 ± 0.2	94.1 ± 0.2
$\theta_{R,15°}$ (°)	68.8 ± 1.5	90.6 ± 1.1
$\theta_{A,90°}$ (°)	–	100.5 ± 2.0
$\theta_{R,90°}$ (°)	–	86.0 ± 4.1

4. Conclusions

In this work, we reproduced the sessile droplet experiment with phase-field simulations based on the finite element method. Initially, we tested the validity of the method on a flat surface by identifying the values of model parameters that lead to physically consistent results, namely the interface thickness ϵ and the mobility parameter M. We then studied the effects of surface micro-structures on the apparent water *CA* (θ) by varying the intrinsic or Young's *CA* (θ_Y) assumed as boundary condition. For the more hydrophobic intrinsic conditions, the results show good agreement with the theoretical Cassie-Baxter state up to the Wenzel transition. Considering the hydrophilic intrinsic condition, instead, the results exhibit a mismatch from the theoretical Wenzel state. We therefore supposed that this discrepancy could be ascribed to the incomplete exhaustiveness of the theoretical models and the possible presence of metastable states that a droplet can explore on non-smooth surfaces. Accordingly, we tested the possible effects of droplet impact velocity to overcome metastable conditions, observing final steady states closer to theoretical predictions.

To validate our numerical studies, we produced and tested a flat and a micro-structured sample. The *CA* on the flat specimen reveals the hydrophilic nature of the sample material (θ_S = 70.4° ± 1.8°). On the other hand, the micro-structure leads to a hydrophobic surface (θ_S = 107.4° ± 4.5°), with water penetration into the interstices between adjacent micro-structures. Similarly, the values of advancing and receding contact angles observed can be attributed to water penetration between the micro-structures. Taking these experimental evidences into account, we performed numerical simulations using the intrinsic contact angle of the specimen material and geometric dimensions comparable to those of the micro-structured sample. The behavior of the simulated system is consistent with the experiments, although there is a slight difference of about 12% in the contact angle. This discrepancy may be due to both experimental and numerical limitations: on the one hand, the geometry of the sample is not perfectly truncated-conical; on the other hand, numerical simulations were performed considering

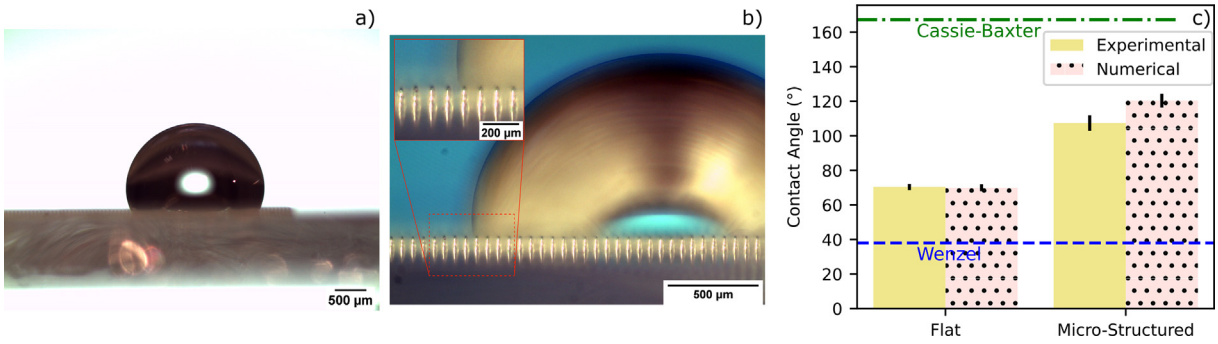

Fig. 6. (a) Sessile droplet experiment on the micro-structured sample. (b) Magnification of the interaction between a water droplet and the micro-structured surface, where it is possible to identify a contrast between the visible background (light blue in the image) and the liquid (yellow in the image) in the areas around the pillars. The image inset shows the color change from left to right of the fifth pillar, transitioning from light blue to yellow. This change corresponds to the contact line of the water droplet with the top of that pillar, highlighting the infiltration phenomenon. (c) Comparison between analytical predictions (Wenzel and Cassie-Baxter models), experimental and numerical results of *CA* for the flat and micro-structured samples. Analytical predictions (Wenzel and Cassie-Baxter lines) were computed assuming that the micro-structures of the sample are reasonably comparable to truncated cones with the geometric properties listed in Table 4, and that the intrinsic wettability of the material is θ_Y = 70.4°.

a 2D domain and other simplifying assumptions. We are therefore considering for future works the use of contact angle dynamic boundary conditions to improve the accuracy of the model. The reliability of numerical simulations is further supported by the water penetration observed in both simulations and experiments.

As also proposed in our previous works [56,57], this study represents a hybrid characterization protocol which can integrate digital and experimental measurements (e.g., coupling CHADA [58] and MODA [59] protocols), assist and speed-up the design process of surfaces with tailored wettability. Furthermore, this work represents a possible final step of a multi-scale model based on the integration with atomistic and mesoscopic simulations, which can provide the boundary conditions for the used continuum model.

Data availability

The numerical raw and processed data required to reproduce these findings are available in the Supplementary Material document and in the MethodsX article associated to this work [22].

Declaration of Competing Interest

The authors declare that they have no known competing financial interests or personal relationships that could have appeared to influence the work reported in this paper.

Acknowledgements

The authors gratefully acknowledge financial support from the European Commission, European project Oyster, www.oyster-project.eu, grant agreement n. 760827. Contact angle measurements were carried out at the "Inter-Departmental Laboratory of Electron Microscopy" (LIME), Universitá degli studi Roma TRE (http://www.lime.uniroma3.it).

Appendix A. Supplementary data

Supplementary data associated with this article can be found, in the online version, at https://doi.org/10.1016/j.matdes.2023.112042.

References

[1] T. Darmanin, F. Guittard, Superhydrophobic and superoleophobic properties in nature, Mater. Today 18 (5) (2015) 273–285, https://doi.org/10.1016/j.mattod.2015.01.001.

[2] M. Chakraborty, J.A. Weibel, J.A. Schaber, S.V. Garimella, The Wetting State of Water on a Rose Petal, Advanced Materials, Interfaces 6 (17) (2019), https://doi.org/10.1002/admi.201900652.

[3] L. Feng, Y. Zhang, J. Xi, Y. Zhu, N. Wang, F. Xia, L. Jiang, Petal Effect: A Superhydrophobic State with High Adhesive Force, Langmuir 24 (8) (2008) 4114–4119, https://doi.org/10.1021/la703821h.

[4] Y. Lin, Y. Shen, A. Liu, Y. Zhu, S. Liu, H. Jiang, Bio-inspiredly fabricating the hierarchical 3D porous structure superhydrophobic surfaces for corrosion prevention, Mater. Des. 103 (2016) 300–307, https://doi.org/10.1016/j.matdes.2016.04.083.

[5] J. Liu, X. Zhang, R. Wang, F. Long, P. Zhao, L. Liu, A mosquito-eye-like superhydrophobic coating with super robustness against abrasion, Mater. Des. 203 (2021), https://doi.org/10.1016/j.matdes.2021.109552 109552.

[6] S.S. Latthe, R.S. Sutar, V.S. Kodag, A.K. Bhosale, A.M. Kumar, K.K. Sadasivuni, R. Xing, S. Liu, Self-cleaning superhydrophobic coatings: Potential industrial applications, Prog. Org. Coat. 128 (2019) 52–58, https://doi.org/10.1016/j.porgcoat.2018.12.008.

[7] M. Ghasemlou, F. Daver, E.P. Ivanova, B. Adhikari, Bio-inspired sustainable and durable superhydrophobic materials: from nature to market, J. Mater. Chem. A 7 (2019) 16643–16670, https://doi.org/10.1039/C9TA05185F.

[8] S.R. Gorthi, H.S. Gaikwad, P.K. Mondal, G. Biswas, Surface tension driven filling in a soft microchannel: role of streaming potential, Ind. Eng. Chem. Res. 59 (9) (2019) 3839–3853, https://doi.org/10.1021/acs.iecr.9b00767.

[9] G.G. Jang, D.B. Smith, G. Polizos, L. Collins, J.K. Keum, D.F. Lee, Transparent superhydrophilic and superhydrophobic nanoparticle textured coatings: comparative study of anti-soiling performance, Nanoscale Adv. 1 (2019) 1249–1260, https://doi.org/10.1039/c8na00349a.

[10] G. Antonetto, M. Morciano, M. Alberghini, G. Malgaroli, A. Ciocia, L. Bergamasco, F. Spertino, M. Fasano, Synergistic freshwater and electricity production using passive membrane distillation and waste heat recovered from camouflaged photovoltaic modules, J. Clean. Prod. 318 (2021), https://doi.org/10.1016/j.jclepro.2021.128464 128464.

[11] M. Alberghini, S. Hong, L.M. Lozano, V. Korolovych, Y. Huang, F. Signorato, S.H. Zandavi, C. Fucetola, I. Uluturk, M.Y. Tolstorukov, et al., Sustainable polyethylene fabrics with engineered moisture transport for passive cooling, Nature Sustain. 4 (8) (2021) 715–724, https://doi.org/10.1038/s41893-021-00688-5.

[12] M. Alberghini, S.V. Boriskina, P. Asinari, M. Fasano, Characterisation and modelling of water wicking and evaporation in capillary porous media for passive and energy-efficient applications, Appl. Therm. Eng. 208 (2022), https://doi.org/10.1016/j.applthermaleng.2022.118159 118159.

[13] S. Zhang, L. Xu, J. Wu, Y. Yang, C. Zhang, H. Tao, J. Lin, L. Huang, W. Fang, K. Shi, et al., Femtosecond laser micro-nano processing for boosting bubble releasing of gas evolution reactions, Nano Res. 15 (2022) 1672–1679, https://doi.org/10.1007/s12274-021-3811-3.

[14] Y. Liu, H. Zhang, P. Wang, Z. He, G. Dong, 3D-printed bionic superhydrophobic surface with petal-like microstructures for droplet manipulation, oil-water separation, and drag reduction, Mater. Des. 219 (2022), https://doi.org/10.1016/j.matdes.2022.110765 110765.

[15] J. Li, W. Fu, B. Zhang, G. Zhu, N. Miljkovic, Ultrascalable three-tier hierarchical nanoengineered surfaces for optimized boiling, ACS Nano 13 (12) (2019) 14080–14093, https://doi.org/10.1021/acsnano.9b06501.

[16] C.-H. Xue, H.-G. Li, X.-J. Guo, Y.-R. Ding, B.-Y. Liu, Q.-F. An, Y. Zhou, Superhydrophobic anti-icing coatings with self-deicing property using melanin nanoparticles from cuttlefish juice, Chem. Eng. J. 424 (2021), https://doi.org/10.1016/j.cej.2021.130553 130553.

[17] W. Xing, Z. Li, H. Yang, X. Li, X. Wang, N. Li, Anti-icing aluminum alloy surface with multi-level micro-nano textures constructed by picosecond laser, Mater. Des. 183 (2019), https://doi.org/10.1016/j.matdes.2019.108156 108156.

[18] Z. Liu, F. Ye, H. Tao, J. Lin, Effects of frost formation on the ice adhesion of micro-nano structure metal surface by femtosecond laser, J. Colloid Interface Sci. 603 (2021) 233–242, https://doi.org/10.1016/j.jcis.2021.06.105.
[19] C. Ge, G. Yuan, C. Guo, C.-V. Ngo, W. Li, Femtosecond laser fabrication of square pillars integrated Siberian-Cocklebur-like microstructures surface for anti-icing, Mater. Des. 204 (2021), https://doi.org/10.1016/j.matdes.2021.109689 109689.
[20] A. Davoudinejad, Y. Cai, D.B. Pedersen, X. Luo, G. Tosello, Fabrication of micro-structured surfaces by additive manufacturing, with simulation of dynamic contact angle, Mater. Des. 176 (2019), https://doi.org/10.1016/j.matdes.2019.107839 107839.
[21] M. Alberghini, M. Morciano, M. Giardino, F. Perrucci, L. Scaltrito, D. Janner, E. Chiavazzo, M. Fasano, P. Asinari, Textured and Rigid Capillary Materials for Passive Energy-Conversion Devices, Adv. Mater. Interfaces (2022), https://doi.org/10.1002/admi.202200057.
[22] M. Provenzano, F.M. Bellussi, M. Morciano, P. Asinari, M. Fasano, Method for predicting the wettability of micro-structured surfaces by continuum phase-field modelling, Submitted to MethodsX.
[23] H.Y. Erbil, The debate on the dependence of apparent contact angles on drop contact area or three-phase contact line: A review, Surf. Sci. Rep. 69 (4) (2014) 325–365, https://doi.org/10.1016/j.surfrep.2014.09.001.
[24] L. Gao, T.J. McCarthy, How Wenzel and Cassie were wrong, Langmuir 23 (7) (2007) 3762–3765, https://doi.org/10.1021/la062634a.
[25] A. Synytska, L. Ionov, V. Dutschk, M. Stamm, K. Grundke, Wetting on Regularly Structured Surfaces from "Core-Shell" Particles: Theoretical Predictions and Experimental Findings, Langmuir 24 (20) (2008) 11895–11901, https://doi.org/10.1021/la8010585.
[26] S. Shibuichi, T. Onda, N. Satoh, K. Tsujii, Super Water-Repellent Surfaces Resulting from Fractal Structure, J. Phys. Chem. 100 (50) (1996) 19512–19517, https://doi.org/10.1021/jp9616728.
[27] J. Bico, U. Thiele, D. Quéré, Wetting of textured surfaces, Colloids Surf., A 206 (1) (2002) 41–46, https://doi.org/10.1016/S0927-7757(02)00061-4.
[28] D. Murakami, H. Jinnai, A. Takahara, Wetting Transition from the Cassie-Baxter State to the Wenzel State on Textured Polymer Surfaces, Langmuir 30 (8) (2014) 2061–2067, https://doi.org/10.1021/la4049067.
[29] L. Zhu, Y. Feng, X. Ye, Z. Zhou, Tuning wettability and getting superhydrophobic surface by controlling surface roughness with well-designed microstructures, Sens. Actuat. A: Phys. 130–131 (2006) 595–600, https://doi.org/10.1016/j.sna.2005.12.005.
[30] P. Mandal, J. Ivvala, H.S. Arora, H.S. Grewal, S.K. Ghosh, Structured aluminium surfaces with tunable wettability fabricated by a green approach, Mater. Lett. 300 (2021), https://doi.org/10.1016/j.matlet.2021.130186 130186.
[31] X. Dai, W. Zhang, J. Zhang, G. Xin, X. Wang, Numerical study of droplet impact on superhydrophobic vibrating surfaces with microstructures, Case Stud. Therm. Eng. 30 (2022), https://doi.org/10.1016/j.csite.2021.101732 101732.
[32] S. Afkhami, Challenges of numerical simulation of dynamic wetting phenomena: a review, Curr. Opin. Colloid Interface Sci. 57 (2022), https://doi.org/10.1016/j.cocis.2021.101523 101523.
[33] Z. Yuan, M. Matsumoto, R. Kurose, Numerical study of droplet impingement on surfaces with hierarchical structures, Int. J. Multiph. Flow 147 (2022), https://doi.org/10.1016/j.ijmultiphaseflow.2021.103908 103908.
[34] B. Narayanan, S.A. Deshmukh, S.K. Sankaranarayanan, S. Ramanathan, Strong correlations between structural order and passive state at water–copper oxide interfaces, Electrochim. Acta 179 (2015) 386–393, https://doi.org/10.1016/j.electacta.2015.03.221.
[35] M. Morciano, M. Fasano, A. Nold, C. Braga, P. Yatsyshin, D. Sibley, B.D. Goddard, E. Chiavazzo, P. Asinari, S. Kalliadasis, Nonequilibrium molecular dynamics simulations of nanoconfined fluids at solid-liquid interfaces, J. Chem. Phys. 146 (24) (2017), https://doi.org/10.1063/1.4986904 244507.
[36] N.T. Chamakos, D.G. Sema, A.G. Papathanasiou, Progress in Modeling Wetting Phenomena on Structured Substrates, Arch. Comput. Methods Eng. 28 (2021) 1647–1666, https://doi.org/10.1007/s11831-020-09431-3.
[37] M. Wörner, Numerical modeling of multiphase flows in microfluidics and micro process engineering: a review of methods and applications, Microfluid. Nanofluid. 12 (6) (2012) 841–886, https://doi.org/10.1007/s10404-012-0940-8.
[38] P. Yue, J.J. Feng, C. Liu, J. Shen, A diffuse-interface method for simulating two-phase flows of complex fluids, J. Fluid Mech. 515 (2004) 293–317, https://doi.org/10.1017/S0022112004000370.
[39] P. Yue, C. Zhou, J.J. Feng, Sharp-interface limit of the Cahn-Hilliard model for moving contact lines, J. Fluid Mech. 645 (2010) 279–294, https://doi.org/10.1017/S0022112009992679.
[40] E. Salvati, F. Menegatti, M. Kumar, M. Pelegatti, A. Tognan, On the significance of diffuse crack width self-evolution in the phase-field model for residually stressed brittle materials, Mater. Des. Process. Commun. 3 (5) (2021), https://doi.org/10.1002/mdp2.261.
[41] C.Y. Lim, Y.C. Lam, Phase-field simulation of impingement and spreading of micro-sized droplet on heterogeneous surface, Microfluid. Nanofluid. 17 (1) (2014) 131–148, https://doi.org/10.1007/s10404-013-1284-8.
[42] L. Zhao, X. Bai, T. Li, J.J.R. Williams, Improved conservative level set method, Int. J. Numer. Meth. Fluids 75 (8) (2014) 575–590, https://doi.org/10.1002/fld.3907.
[43] T. Wang, G. Liang, L. Li, S. Zhou, S. Shen, Droplet Wetting Propagation on a Hybrid-Wettability Surface, Langmuir 37 (39) (2021) 11646–11656, https://doi.org/10.1021/acs.langmuir.1c02255.
[44] J. Hu, X. Xiong, H. Xiao, K.-T. Wan, Effects of Contact Angle on the Dynamics of Water Droplet Impingement, Excerpt from the Proceedings of the 2015 COMSOL Conference in Boston.
[45] D. Jacqmin, Calculation of Two-Phase Navier-Stokes Flows Using Phase-Field Modeling, J. Comput. Phys. 155 (1) (1999) 96–127, https://doi.org/10.1006/jcph.1999.6332.
[46] F. Bai, X. He, X. Yang, R. Zhou, C. Wang, Three dimensional phase-field investigation of droplet formation in microfluidic flow focusing devices with experimental validation, Int. J. Multiph. Flow 93 (2017) 130–141, https://doi.org/10.1016/j.ijmultiphaseflow.2017.04.008.
[47] COMSOL Multiphysics v. 5.6.
[48] P. Johansson, B. Hess, Molecular origin of contact line friction in dynamic wetting, Phys. Rev. Fluids 3 (7) (2018), https://doi.org/10.1103/PhysRevFluids.3.074201.
[49] D. Jacqmin, Contact-line dynamics of a diffuse fluid interface, J. Fluid Mech. 402 (2000) 57–88, https://doi.org/10.1017/S0022112099006874.
[50] P. Yue, J.J. Feng, Wall energy relaxation in the Cahn-Hilliard model for moving contact lines, Phys. Fluids 23 (2011), https://doi.org/10.1063/1.3541806 012106.
[51] J. Hu, R. Jia, K.-T. Wan, X. Xiong, Simulation of Droplet Impingement on a Solid Surface by the Level Set Method, Excerpt from the Proceedings of the 2014 COMSOL Conference in Boston.
[52] D. Wang, Q. Sun, M.J. Hokkanen, C. Zhang, F.-Y. Lin, Q. Liu, S.-P. Zhu, T. Zhou, Q. Chang, B. He, Q. Zhou, L. Chen, Z. Wang, R.H.A. Ras, X. Deng, Design of robust superhydrophobic surfaces, Nature 582 (2020) 55–59, https://doi.org/10.1038/s41586-020-2331-8.
[53] A. Tuteja, W. Choi, G.H. McKinley, R.E. Cohen, M.F. Rubner, Design Parameters for Superhydrophobicity and Superoleophobicity, MRS Bull. 33 (2008) 752–758, https://doi.org/10.1557/mrs2008.161.
[54] M. Santini, M. Guilizzoni, S. Fest-Santini, X-ray computed microtomography for drop shape analysis and contact angle measurement, J. Colloid Interface Sci. 409 (2013) 204–210, https://doi.org/10.1016/j.jcis.2013.06.036.
[55] W. Yanling, Y. Jian, Y. Huadong, Superhydrophobic surface prepared by micro-milling and WEDM on aluminum alloy, Mater. Res. Exp. 5 (6) (2018), https://doi.org/10.1088/2053-1591/aac6a3 066504.
[56] A. Cardellini, F.M. Bellussi, E. Rossi, L. Chiavarini, C. Becker, D. Cant, P. Asinari, M. Sebastiani, Integrated molecular dynamics and experimental approach to characterize low-free-energy perfluoro-decyl-acrylate (PFDA) coated silicon, Mater. Des. 208 (2021), https://doi.org/10.1016/j.matdes.2021.109902 109902.
[57] F.M. Bellussi, O.M. Roscioni, E. Rossi, A. Cardellini, M. Provenzano, L. Persichetti, V. Kudryavtseva, G. Sukhorukov, P. Asinari, M. Sebastiani, et al., Wettability of soft PLGA surfaces predicted by experimentally augmented atomistic models, MRS Bull. (2022), https://doi.org/10.1557/s43577-022-00380-9.
[58] European Committee for Standardization, CEN Workshop Agreement CWA 17815: Materials characterisation - Terminology, metadata and classification, URL:https://www.cencenelec.eu/media/CEN-CENELEC/CWAs/ICT/cwa17815.pdf (2021).
[59] European Committee for Standardization, CEN Workshop Agreement CWA 17284: Materials modelling – Terminology, classification and metadata, URL: https://www.cencenelec.eu/media/CEN-CENELEC/CWAs/RI/cwa17284_2018.pdf (2018).